JOURNAL OF AIRCRAFT
Vol. 46, No. 5, September–October 2009

Prediction of Helicopter Maneuver Loads Using a Fluid–Structure Analysis

Jayanarayanan Sitaraman* and Beatrice Roget†
National Institute of Aerospace, Hampton, Virginia 23666-6147

DOI: 10.2514/1.43004

A fluid–structure analysis framework that couples computational fluid dynamics and computational structural dynamics is constructed to study the aeromechanics of a helicopter rotor system under maneuvering-flight conditions. The computational fluid dynamics approach consists of the solution of unsteady Reynolds-averaged Navier–Stokes equations for the near field of the rotor coupled with the dynamics of trailed vortex wake that is computed using a free-vortex method. The computational structural dynamics approach uses a multibody finite element method to model the rotor hub and blades. The analysis framework is used to study the utility tactical transport aerial system pull-up maneuver of the UH-60A helicopter. Results shown illustrate the correlation of predicted performance, aerodynamic and structural dynamic loading, with measured flight-test data. The normal load factor and the peak-to-peak structural and aerodynamic loading show good correlation with flight-test data, indicating that the analysis framework is suitable for preliminary design purposes. Important phenomena such as advancing-blade transonic effects and retreating blade flow separation are predicted satisfactorily. However, deficiencies are noted in the accurate prediction of stall onset, reattachment, and shock-induced separation.

I. Introduction

HELICOPTER rotor systems operate in highly unsteady flow conditions that are characterized by transonic flows, dynamic stall events, and returning-wake interactions. In addition, there is a large extent of aeroelastic coupling, due to the slender construction of the blades. All of these factors contribute to make the prediction of aerodynamic and structural dynamic loading on helicopter rotors a very challenging problem, even in steady forward flight. Maneuvering rotorcraft further augments this challenge because of additional aerodynamic and structural effects due to the hub motion and associated wake transients.

The simulation tools for rotorcraft analysis (termed comprehensive aeroelastic analyses) have historically been using lifting-line-based aerodynamic models (with suitable enhancements that use table lookup, unsteady flow, and stall models). However, such models are known to have inaccurate prediction capabilities [1]. There are two main reasons for the inaccuracies in the lifting-line models. The first is the inability to resolve unsteady transonic effects, and the second is the inability to accurately resolve the returning-wake effects [2]. The advent of the computational fluid dynamics (CFD) and computational structural dynamics (CSD) coupled approach replaces the lifting-line aerodynamic model with a higher-fidelity computational fluid dynamic model that solves the Reynolds-averaged Navier–Stokes (RANS) equations. This methodology has led to considerable improvements in the airload prediction, as demonstrated by various research efforts [2–6]. The primary reason for the improvement can be attributed to accurate prediction of aerodynamic loading, especially the pitching moments caused by unsteady transonic flows and improved representation of returning-wake effects [3].

An important aspect of CFD-based aerodynamic load prediction methodologies is the resolution of the wake structures. There are two well-established methodologies that are in use at the moment for wake predictions. They are 1) wake coupling [7] and 2) wake capturing [3,4,8]. In the wake-coupling methodology, the geometry of the vortex wake, circulation strength, and core growth rate are computed externally by solving the vorticity transport equation. The wake positions so obtained are embedded into the RANS-based CFD analysis using the field-velocity approach [9]. The wake-capturing methodology, in contrast, models the entire rotor system and attempts to capture the wake structure as part of the solution. The advantages of the wake-coupling methodology are computational efficiency and ease of modeling. However, it suffers from the empiricism that is used to model the physical diffusion of vorticity. The wake-capturing methodology has the advantage of being a first-principle-based modeling technique without any empiricism. However, it does suffer from high computational cost and numerical diffusion in predicting the wake structure. An evaluation of the wake-coupling and wake-capturing methodologies for prediction of steady-flight conditions can be found in [10]. Several flight conditions that address flow phenomena such as transonics, stall, and blade–vortex interactions were studied in this work. It was observed that the wake-coupling approach produced results of comparable quality as the wake-capturing approach for all of the flight conditions that were studied.

The main focus of most recent research efforts was on predicting rotor airloads in steady-flight conditions. The periodic nature of the flowfield and structural response facilitates the use of the so-called loose-coupling approach for interfacing the CFD and CSD analysis modules. In the loose-coupling approach, the analysis modules exchange relevant data only every rotor revolution. The inherent decoupling within a revolution provides a fast and robust way for establishing aircraft trim and a fully periodic structural response. In contrast, simulating an unsteady helicopter maneuver necessitates the exchange of forces and motions at every time step between the fluid and structure methodologies.

Recently, Bhagwat et al. [11] and Bhagwat and Ormiston [12] performed the seminal studies on computing airloads and blade loads for the UH-60A pull-up maneuver using a CFD/CSD analysis that coupled OVERFLOW-2 (wake-capturing CFD) and RCAS (CSD and comprehensive analysis) [4]. Remarkable improvements were demonstrated in the prediction of aerodynamic and structural dynamic loads compared with conventional comprehensive analysis. This study triggered a lot of interest in the application of CFD/CSD

Received 1 January 2009; accepted for publication 26 May 2009.

*Research Scientist, 100 Exploration Way; jaina@nianet.org. Member AIAA.

†Research Scientist, 100 Exploration Way; broget@nianet.org. Member AIAA.

coupling analysis to simulate helicopter maneuvering flight. Abhishek et al. [13] coupled a simplified aerodynamic model with multibody CSD analysis. The results obtained were satisfactory for peak-to-peak loading, especially for the push-rod loads; however, the details of loading waveforms showed unexplained phase differences. Silbaugh and Baeder [14] used a wake-capturing CFD approach coupled with a simplified structural dynamic model. This study concentrated on isolating the differences between the time-accurate and serial-staggered coupling approaches and performed simulations only for the first 15 revolutions of the maneuver.

The objective of the present work is to further validate and enhance the analytical approach by constructing an analysis platform composed of another set of CFD/CSD analysis tools (UMTURNS [10,15] for CFD and DYMORE [16] for CSD). There are two main differences in the analysis framework used in this paper compared with that used by Bhagwat et al. [11]. The wake-coupling methodology is used here in contrast to the wake-capturing methodology. In addition, the coupling of codes is performed using a Python-based framework in which all data exchange is performed using memory pointers rather than file I/O, making the coupling process efficient and seamless. The time evolution of the structural, fluid dynamic, and vorticity transport equations are consistently coupled to obtain an aeroelastic solution for the unsteady maneuver.

II. Methodology

A. CFD Solver

The Navier–Stokes equations are solved in their Reynolds-averaged form, which has been proven to be well-suited for high-Reynolds-number external-flow problems, as in the case of helicopter flight. After Reynolds averaging, the Navier–Stokes equations govern the variation of the mean (time-averaged) flow quantities. Closure is achieved by accounting for turbulent fluctuations that are found using an adequate model that is dependent on the mean quantities (algebraic or equation-based).

The RANS solver used as the CFD analysis is the University of Maryland TURNS code [3,8], which operates on meshes that follow structured-curvilinear topology. The UMTURNS code uses a finite volume numerical algorithm that evaluates the inviscid fluxes using an upwind-biased flux difference scheme. The van Leer monotone upstream-centered scheme for conservation laws (MUSCL) approach is used to obtain third-order accuracy, with Koren's differentiable flux limiters to make the scheme total-variation-diminishing. Viscous fluxes are computed using a fourth-order central-difference discretization. The Spalart–Allmaras one-equation model is used for the turbulence closure. The turbulence model equations are solved while segregated from the mean-flow solutions, and the necessary implicitness and time accuracy are achieved using subiterations.

The lower–upper symmetric Gauss–Seidel (LU-SGS) scheme suggested by Jameson and Yoon [17] and Yoon and Jameson [18] is used for the implicit operator. Briefly, the LU-SGS method is a direct modification of the approximate lower–diagonal–upper factorization to the unfactored implicit matrix. Though the (LU-SGS) implicit operator increases the stability and robustness of the scheme, the use of a spectral radius approximation renders the method only first-order-accurate in time. Therefore, a second-order backward difference in time is used, along with Newton-type subiterations to restore formal second-order time accuracy.

UMTURNS uses the arbitrary Lagrangian–Eulerian (ALE) formulation for modeling unsteady flows with motion of the solid surfaces, as in the case of helicopter flows. Calculations of the space and time metrics are the key requirements for the ALE formulation. The present numerical scheme employs a modified finite volume method for calculating the space and time metrics. Finite volume formulations have the advantage that both the space and time metrics can be formed accurately and freestream is captured accurately [19]. Also, it is to be noted that the computations include not only aeroelastic deformations but also gust fields that are generated by hub motion and wake transients. The space and time metrics are evaluated in such a manner that they implicitly satisfy the geometric conservation law and also maintain the order of accuracy of the numerical scheme [9].

The computational domain is partitioned to facilitate calculations in a distributed computing environment. All parallel communications are achieved using the message-passing interface (MPI-2) standard.

1. *Calculation of Space and Time Metrics*

The strong conservation-law form of the Navier–Stokes equations in Cartesian coordinates can be written as [20]

$$\begin{aligned} &q_t + f_x + g_y + h_z = \sigma_x + \theta_y + \omega_z \qquad q = (\rho, \rho u, \rho v, \rho w, \rho E)^T \\ &E = e + \frac{u^2 + v^2 + w^2}{2} \qquad f = (\rho u, p + \rho u^2, \rho uv, \rho uw, \rho uH)^T \\ &g = (\rho v, \rho vu, p + \rho v^2, p + \rho vw, \rho vH)^T \\ &h = (\rho w, \rho wu, \rho wv, p + \rho w w^2, \rho wH)^T \qquad H = E + p/\rho \end{aligned} \tag{1}$$

where subscripts indicate partial differentiation; t is the physical time; u, v, and w are the velocity components in the coordinate directions x, y, and z; ρ is the density; p is the pressure; e the specific internal energy; and σ, θ, and ω represent the viscous stress and work terms for each coordinate direction. Upon transforming to computational coordinates ξ, η, and ζ and nondimensional time τ with the aid of the chain rule of partial derivatives, Eq. (1) becomes

$$\begin{aligned} &\hat{q}_\tau + \hat{f}_\xi + \hat{g}_\eta + \hat{h}_\zeta = \hat{\sigma}_\xi + \hat{\theta}_\eta + \hat{\omega}_\zeta \qquad \hat{q} = Jq \\ &\hat{f} = \hat{\xi}_t q + \hat{\xi}_x f + \hat{\xi}_y g + \hat{\xi}_z h \qquad \hat{\sigma} = \hat{\xi}_x \sigma + \hat{\xi}_y \theta + \hat{\xi}_z \omega \\ &\hat{g} = \hat{\eta}_t q + \hat{\eta}_x f + \hat{\eta}_y g + \hat{\eta}_z h \qquad \hat{\theta} = \hat{\eta}_x \sigma + \hat{\eta}_y \theta + \hat{\eta}_z \omega \\ &\hat{h} = \hat{\zeta}_t q + \hat{\zeta}_x f + \hat{\zeta}_y g + \hat{\zeta}_z h \qquad \hat{\omega} = \hat{\zeta}_x \sigma + \hat{\zeta}_y \theta + \hat{\zeta}_z \omega \end{aligned} \tag{2}$$

Here, terms of the form $\hat{\xi}_{x,y,z}$, $\hat{\eta}_{x,y,z}$, and $\hat{\zeta}_{x,y,z}$ are the space metrics, $\hat{\xi}_t$, $\hat{\eta}_t$, and $\hat{\zeta}_t$ are the time metrics in the computational domain, and J is the Jacobian of the inverse coordinate transformation: that is,

$$J = \det\left(\frac{\partial(x, y, z)}{\partial(\xi, \eta, \zeta)}\right)$$

2. *Field-Velocity Approach*

For the computations presented here, the vortex wake is computed using time-accurate solutions of the vorticity transport equation. The effect of vortex wake is then coupled to the fluid equations using the field-velocity approach [9], which is a way of modeling external velocity fields via apparent grid movement.

Mathematically, the field-velocity approach can be explained by considering the velocity field $\mathbf{V}$ in the physical Cartesian domain. It can be written as

$$\mathbf{V} = (u - x_\tau)\mathbf{i} + (v - y_\tau)\mathbf{j} + (w - z_\tau)\mathbf{k} \tag{3}$$

where $\mathbf{i}$, $\mathbf{j}$, and $\mathbf{k}$ are unit vectors along the three Cartesian coordinate directions; u, v, and w are components of the velocity along the coordinate directions; and x_τ, y_τ, and z_τ are the corresponding grid velocity component. Let the velocity induced by the external potential (e.g., that generated by the vortex wake) be represented by a velocity field (u', v', w'). Thus, the velocity field becomes

$$\mathbf{V} = (u - x_\tau + u')\mathbf{i} + (v - y_\tau + v')\mathbf{j} + (w - z_\tau + w')\mathbf{k} \tag{4}$$

The field-velocity approach models this changed velocity field by changing the grid velocities. The modified grid velocities are defined as

$$\tilde{x}_\tau \mathbf{i} + \tilde{y}_\tau \mathbf{j} + \tilde{z}_\tau \mathbf{k} = (x_\tau - u')\mathbf{i} + (y_\tau - v')\mathbf{j} + (z_\tau - w')\mathbf{k} \tag{5}$$

Once the modified grid velocities are obtained, the grid time metrics in the computational domain $(\hat{\xi}_t, \hat{\eta}_t, \hat{\zeta}_t)$ are computed as

$$\hat{\xi}_t = -(\hat{\xi}_x \tilde{x}_\tau + \hat{\xi}_y \tilde{y}_\tau + \hat{\xi}_z \tilde{z}_\tau) \qquad \hat{\eta}_t = -(\hat{\eta}_x \tilde{x}_\tau + \hat{\eta}_y \tilde{y}_\tau + \hat{\eta}_z \tilde{z}_\tau)$$
$$\hat{\zeta}_t = -(\hat{\zeta}_x \tilde{x}_\tau + \hat{\zeta}_y \tilde{y}_\tau + \hat{\zeta}_z \tilde{z}_\tau) \tag{6}$$

Detailed validation of this approach for model problems as well as full helicopter simulations can be found in [9].

B. CSD Solver

In the present study, the CSD code DYMORE is used for structural modeling. DYMORE is a finite-element-based tool for the analysis of nonlinear elastic multibody systems, developed at the School of Aerospace Engineering, Georgia Institute of Technology (Bauchau and Kang [16]). It includes a library of structural elements from which models with arbitrarily complex topologies can be built. The element library includes rigid bodies, cables, composite capable beams and shells, and joint models, can include generic spring and/or damper elements. Deformable bodies are modeled with the finite element method. The formulation of beams is geometrically exact (i.e., arbitrarily large displacements and finite rotations are accounted for) but is limited to small strains. The equations of equilibrium are written in a Cartesian inertial frame. Constraints are modeled using the Lagrange multiplier technique, resulting in a system of differential/algebraic equations. These equations are then solved using a robust and efficient time integration algorithm [21].

C. Time-Accurate Wake Computations

The aerodynamic model incorporated in DYMORE uses 2-D airfoil theory augmented with airfoil table lookup. The inflow model is based on the theory for unsteady flow over a circular disk with a pressure jump across that disk [22]. In the present work, a free-wake analysis is devised in an attempt to improve the inflow modeling and enhance the accuracy of rotor aerodynamics predictions.

The dominant structures in the rotor flowfield are the blade tip vortices. The present analysis considers a single-tip vortex filament on each lifting line of a rotor, released from each blade tip. The free-wake problem is governed by the vorticity transport equation. Assuming that vortex elements convect with the fluid particles, the equation of evolution for the wake markers can be written as

$$\frac{\mathrm{d}\mathbf{r}(\psi,\zeta)}{\mathrm{d}t} = \mathbf{V}(\mathbf{r}(\psi,\zeta)) \tag{7}$$

where $\mathbf{r}$ defines the position vector of a wake marker, located on a vortex filament that is trailed from a rotor blade located at an azimuth ψ, and was first created when the blade was located at an azimuth $(\psi - \zeta)$, as represented in Fig. 1. The vorticity transport equation can be written in the following partial differential form:

$$\frac{\partial \mathbf{r}(\psi,\zeta)}{\partial \psi} + \frac{\partial \mathbf{r}(\psi,\zeta)}{\partial \zeta} = \frac{\mathbf{V}(\mathbf{r}(\psi,\zeta))}{\Omega} \tag{8}$$

where Ω is the hub rotational velocity. The right-hand-side velocity accounts for the instantaneous velocity field encountered by a marker on a vortex filament in the rotor wake. This includes the freestream velocity, the induced velocities due to all the vortex filaments present in the wake, and the induced contributions of the bound circulation representing the lifting rotor blades. This equation must be discretized into a set of finite difference equations that can then be numerically integrated. The time-marching algorithm chosen is based on that suggested in [23] and is modified to suit the present analysis framework [24].

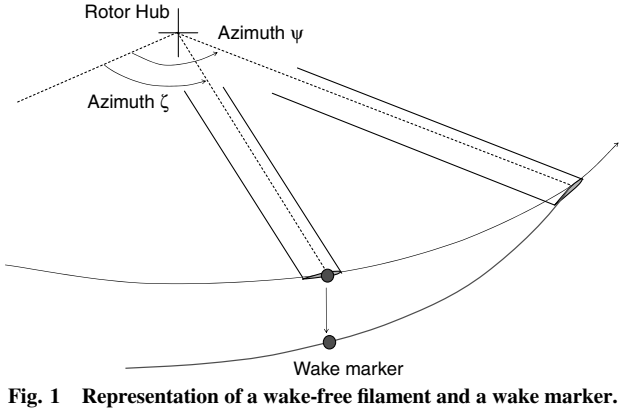

Fig. 1 Representation of a wake-free filament and a wake marker.

The velocity term in the vorticity transport equation is computed from the Biot–Savart law:

$$\mathbf{V}(r) = \frac{\Gamma}{4\pi} \frac{h^2}{\sqrt{h^2 + r_c^2}} \int \frac{\mathrm{d}\boldsymbol{l} \times \mathrm{d}\mathbf{r}}{|\mathbf{r}|^3} \tag{9}$$

where $\mathbf{V}(r)$ is the velocity induced at a point P located at r relative to the vortex element $d\boldsymbol{l}$. The integral is evaluated over the entire length of the vortex filament. Γ is the total strength of the filament, and $d\boldsymbol{l}$ is an elemental unit vector along the vortex filament. The vortex core radius is noted as r_c, and h is the perpendicular distance of the evaluation point from the influencing vortex element. Viscous diffusion is modeled by the growth of the core radius given by [25]

$$r_c(\zeta) = \sqrt{r_{\text{initial}}^2 + 4\alpha\delta\nu\zeta/\Omega} \tag{10}$$

where α is an empirical factor ($\alpha = 1.25643$), δ is the apparent viscosity coefficient, and ν is the kinematic viscosity. The circulation Γ released at the blade tip is assumed to be equal to the maximum bound circulation along the blade. A near wake is included in the model to improve the accuracy of modeling the distortions created by the blades on the trailed vortex wake. The blade bound circulation is fixed at the blade quarter-chord and the near-wake trailers emanate from these locations. For operations within a table-lookup-based aerodynamic modeling, the blade bound circulations are computed by enforcing flow boundary conditions at the control points that are located at the three-quarter-chord location. This method provides a good first approximation to a lifting-surface analysis and is more accurate than a lifting-line analysis [26]. For coupled operation with CFD, the blade bound circulations are computed directly from the CFD aerodynamic loading.

After the velocity contributions [Eq. (9)] from both near and far wakes are evaluated and aggregated at each wake marker location, the ordinary differential equations that denote the evolution of the wake markers are integrated in time using a second-order backward predictor–corrector algorithm (see the Appendix in [24]).

D. Fluid–Structure Interface

Because rotor blades have very little elasticity in the chordwise direction, they can be modeled quite accurately in the CSD methodology using a 1-D beam representation with flap, lag, axial, and torsion degrees of freedom. In contrast, the entire surface of the blade is represented in the CFD mesh within the limit of grid resolution. The difference in geometry description of the CFD and CSD models requires specialized formulation for the transfer of loads and displacements. In this paper, we follow a rather simple approach of one-dimensional interpolation of sectional aerodynamic loading using cubic splines. Because of the structured nature of the grid, sectional aerodynamic loading can be easily determined using the pressure and shear stress distributions on the CFD surface grid. These are interpolated using cubic spline interpolation to the control points of the CSD model. As the spanwise resolution of the CFD mesh is commensurate (slightly higher) with that of the CSD control point distribution there is very little inconsistency between the total loading integrated in either solver (i.e., this method is force-preserving within the limit of grid resolution). Additionally, local continuity of loading is maintained because force/unit length is interpolated as opposed to the lumped force itself.

E. CFD-Wake Interface

The Eulerian fluid dynamic equations (1) and Lagrangian wake equations (8) are interfaced using the field-velocity approach. At any time step, the wake coordinates obtained from the wake solver are

used to evaluate the induced-velocity field (u', v', w') at every grid point. The computation of the induced-velocity field is quite expensive if a direct naive approach is followed. Therefore, we use a fast hierarchical approach [9] to accelerate this calculation, which brings the associated computational overhead down to only about 10% of the total time step. Note that to prevent doubly accounting for the near-wake region (i.e., region directly behind the blade), all of the wake filaments that belong to a particular blade and are contained inside the CFD mesh belonging to that blade are not included in the induced-velocity calculations.

The CFD aerodynamic loading on the blade determines the bound vorticity and hence the amount of vorticity shed into the wake markers, as described in Sec. II.C. In essence, the wake solver gives the wake positions, their circulation strengths, and vortex diffusion parameters to the CFD solver. The CFD solver in turn provides the sectional aerodynamic loading to the wake solver such that the appropriate bound-vorticity profile can be computed.

F. Time Integration Procedure

The fluid, structure, and wake equations are integrated using the conventional serial-staggered (CSS) time-stepping scheme, as shown in Fig. 2. The CSS scheme was shown to provide similar levels of accuracy as a fully-time-accurate simulation (subiteration based) for a smaller computational overhead by Silbaugh and Baeder [14]. Therefore, this method is adopted for the present study. The sequence of integration is as follows: first the CSD solver computes converged blade position using the provided aerodynamic loading; following that, the wake solver computes new wake locations based on this new blade position as well as the provided aerodynamic loading. Once the new blade positions and wake locations are obtained, the fluid equations are integrated to generate the aerodynamic loading for the next time step. Note that this method not only degrades in accuracy but also shows instabilities if large time steps are used. In the present work, an azimuthal step of 0.4 deg is used. This value results in a similar level of overall accuracy when using the serial-staggered scheme compared with the fully-time-accurate simulation.

The initiation of the fluid–structure solution often creates large transients in both physical systems that can be amplified by the combined time integration procedure (because of its explicit nature), leading to destabilization. To prevent such destabilization from occurring, the CFD-based aerodynamic loading is slowly introduced into the CSD loading using a smooth cosine decay scheme. The aerodynamic model (lifting-line based) is kept active in the CSD solver for the initiation. This model is fully coupled in the subiteration level and does not cause destabilization. Twelve revolutions of CFD/CSD coupling under steady-forward-flight operating conditions are simulated before initiating the pull-up maneuver to ensure solution periodicity and complete damping of initial transients. The aerodynamic loading from the CFD is slowly mixed with the lifting-line aerodynamic loading over a half-revolution of this steady-flight simulation. After the first half-revolution the lifting-line modeling is completely turned off and the CSD loading is exactly equal to the CFD aerodynamic loading.

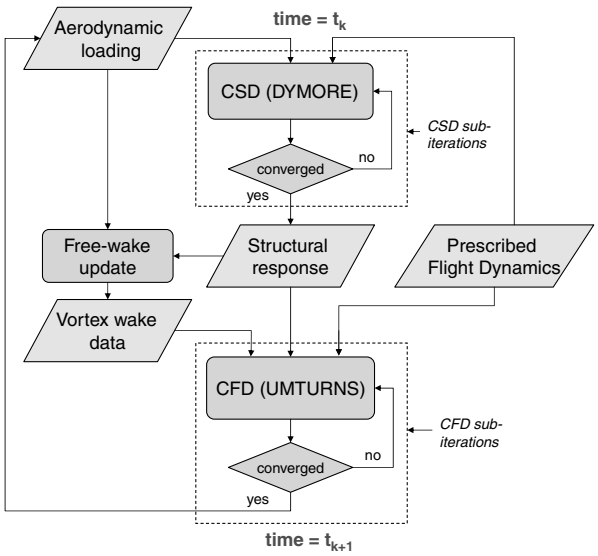

Fig. 2 Schematic of the time-stepping sequence used for integration of governing fluid, wake and structural dynamic equations of the unsteady maneuver problem.

G. Python-Based Coupling Framework

The data transfer between the CFD and CSD/Freewake codes are facilitated in a Python-based framework. Python supports object-oriented programming, and each participating solver is treated as an object (or module, in FORTRAN90 parlance). The infrastructure executes legacy solvers but only after the solvers are wrapped with a socketlike Python layer. Python interfaces are compatible with other programming languages, and there are freely available tools for developing these Python interfaces, such as f2py and swig for codes in FORTRAN90 and C/C++, respectively. Once wrapped, the participating solvers execute largely independently of one another, following their own native parallel implementation. Different solvers can reference each other's data through the Python layer using standard C-like pointers, without memory copies or file I/O. However, the different solvers must accommodate common shared data structures maintained at the Python level for this to work efficiently. In essence, after the necessary wrapping procedures, the Python script becomes the driver for the entire CFD/CSD simulation and orchestrates the appropriate time-stepping and data exchange paradigms. In addition, it is also possible to run the Python wrapped code in parallel under MPI using pyMPI or mympi, allowing one to use the large-scale parallel computers that are traditionally used for large-scale CFD calculations.

H. UH-60A Aerodynamic and Structural Dynamic Models

The mesh system used for the UH-60A rotor follows a C-O topology and is shown in Figs. 3 and 4. The finest grid used for each rotor blade has 325 points in the wraparound direction, 145 points in the spanwise direction, and 129 points in the normal direction, respectively. The outer boundary of the grid extends about three chords from the blade surface. The full mesh system uses four such grids, one for each rotor blade. Finer-grid clustering is used in regions of high gradients such as the shed-wake region (directly behind the trailing edge of the blade) and trailed-wake region (at the root and tip of the blade). The wake-coupling approach described in the previous section is used for including the returning-wake effects.

Figure 5 shows a representation of the UH-60 rotor modeled using DYMORE. The rotor model consists of four elastic blades, each using 15 elements with cubic shape functions. The blade root articulation is modeled using three revolute joints, coincident at 4.66% blade radius. A rigid model of the rotor control system is used,

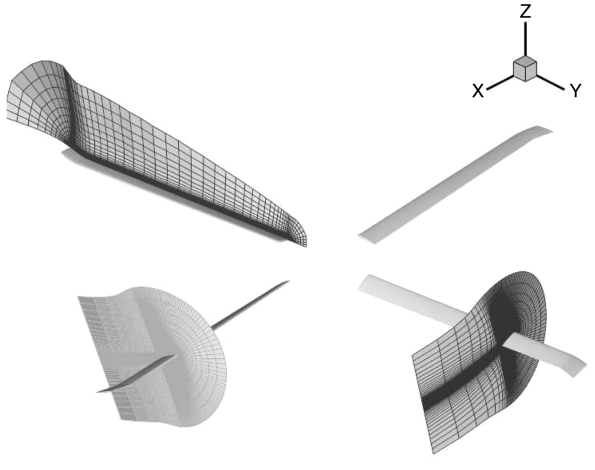

Fig. 3 Mesh topology for UMTURNS wake-coupling methodology.

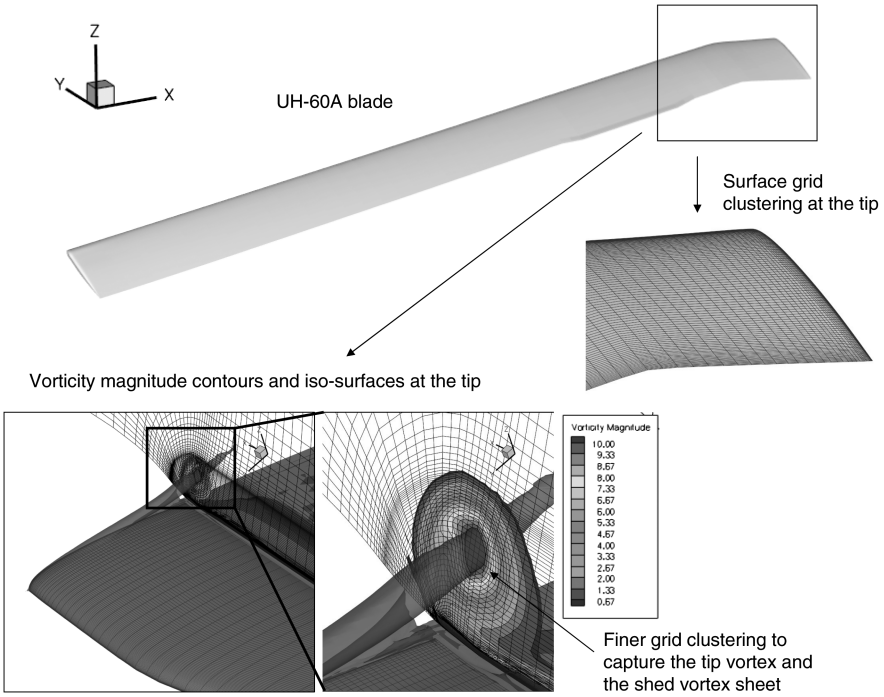

Fig. 4 Details of finer-grid clustering used in regions of high gradients.

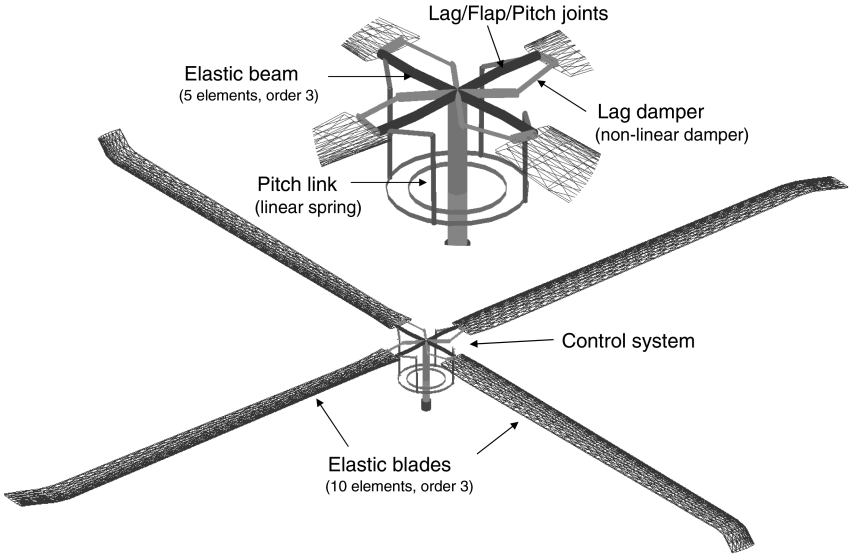

Fig. 5 Details UH-60A structural model used in DYMORE.

including the push rods, pitch horns, and rotating and fixed swash plates. The push rods are modeled as rigid elements connected to a prismatic joint with linear stiffness equal to $187,792$ lb/ft [11]. A model of the lead-lag damper is also included by modeling the damper as a rigid element connected to a prismatic joint with nonlinearly varying damping coefficient.

1. *Validation of Aerodynamic Modeling*

Figure 6 illustrates the improved prediction capabilities of the CFD-based aerodynamic modeling compared with traditional lifting-line-based capabilities that are part of comprehensive analysis codes. Results are shown for the high-speed flight condition of the UH-60A helicopter. An identical set of blade motions that are obtained by forcing the structural model with measured flight-test data is used for computation of aerodynamic loading in both lifting-line and CFD approaches. The plots shown consist of aerodynamic loading (normal force and pitching moment) variation toward the tip of the rotor and are representative of the overall quality of the results. It is evident that the CFD-based aerodynamic modeling shows much improved agreement with experimental data for both normal force and pitching moment waveforms.

2. *Validation of Structural Dynamic Model*

The rotor blade frequency plot is shown in Figs. 7a and 7b, which correspond to two different values of push-rod stiffness, $62,631$ lb/ft and $187,792$ lb/ft, respectively. The larger stiffness value has been suggested as being more accurate and is the one used in the present analysis [11]. However, the frequency variation results are presented for both stiffness values to allow comparison with published results using different comprehensive analysis [27,28]. The predicted natural blade frequencies compare well with results from other analyses. The main effect of stiffening the push rod is to increase the first torsional frequency from about 3.8/rev to about 4.2/rev. Other natural frequencies are not significantly affected.

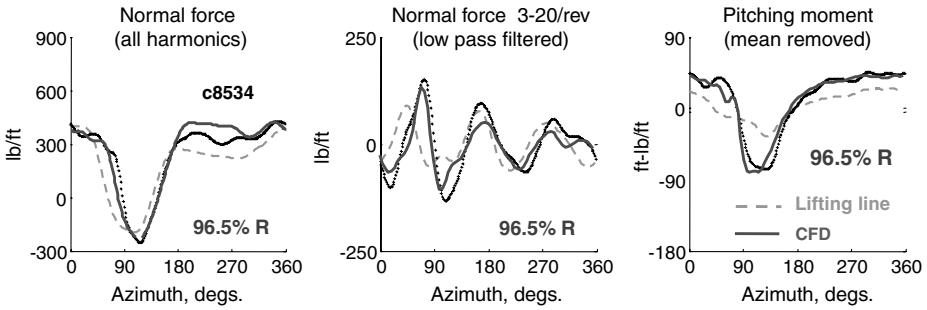

Fig. 6 Comparison of aerodynamic loading obtained from CFD and lifting-line models for high-speed forward flight condition (advance ratio, $\mu = 0.368$).

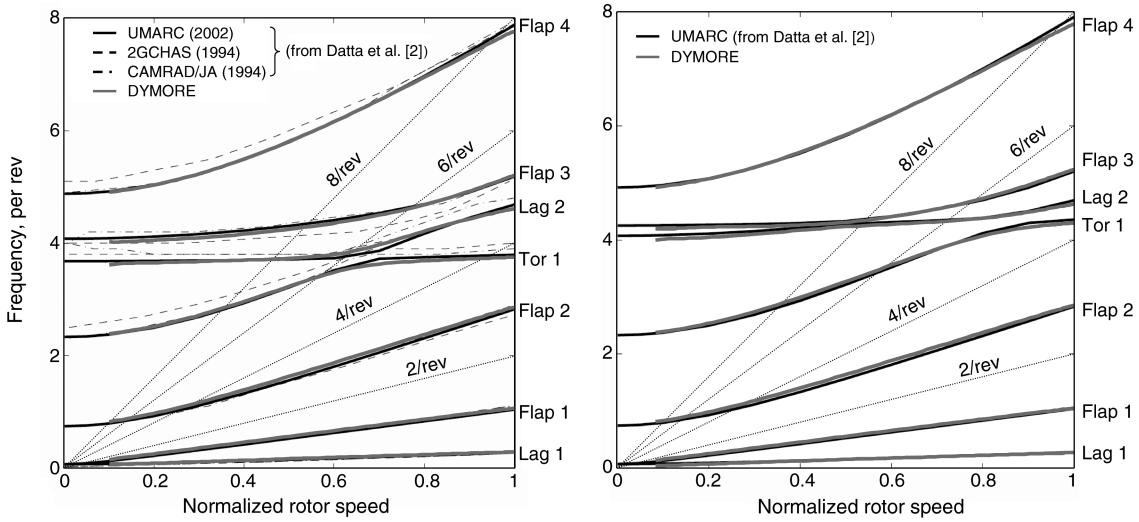

a) Rooting spring stiffness = 62631 lbs/ft **b) Rooting spring stiffness = 187792 lbs/ft**

Fig. 7 Rotor frequency plot of the UH-60A rotor obtained using the DYMORE structural dynamic model compared with those obtained from University of Maryland Advanced Rotorcraft Code [27].

III. UH-60A 11029 Maneuver Description

The NASA and U.S. Army UH-60A Airloads Program investigated a wide range of flight conditions. Detailed measurements of blade aerodynamics and structural dynamics load measurements were conducted, which serve as a rich database for code validation. An extensive documentation of the flight-test program can be found in [29,30]. The operating envelope of the helicopters plotted as variation of vehicle weight coefficient with advance ratio is shown in Fig. 8. The limiting factors for these flight conditions are the maximum thrust limit because of retreating blade stall and the maximum sectional airfoil lift that can be generated. McHugh [31] determined the maximum thrust boundary using wind-tunnel tests, which is represented in the figure. Note that all the steady-flight conditions lie below the McHugh boundary. Figure 8 also shows the variation of weight coefficient with advance ratio for the Utility Tactical Transport Aircraft System (UTTAS) pull-up maneuver. The maneuver begins quite closely to the maximum level-flight speed of the aircraft and achieves a peak load factor of 2.1 g, which exceeds the steady-state McHugh boundary. Therefore, the UTTAS pull-up maneuver is a challenging flight condition in terms of predictive capability. A schematic of the UH-60A pull-up maneuver is also shown in Fig. 8, which consists of a transition from a level-flight condition to a steady-climb condition in about 40 revolutions of the rotor (approximately 10 s).

IV. Maneuver Analysis

Simulation of free-flight maneuver requires the inclusion of a flight dynamic model in the calculation of the aeroelastic response of the complete rotorcraft. A few simplifications are introduced in the present study to reduce the complexity of the entire problem and facilitate validation. First, the pitch control inputs are prescribed rather than calculated in this analysis. Second, only the longitudinal dynamics of the maneuver is prescribed, as it is the dominant contributor to the fundamental physical mechanisms.

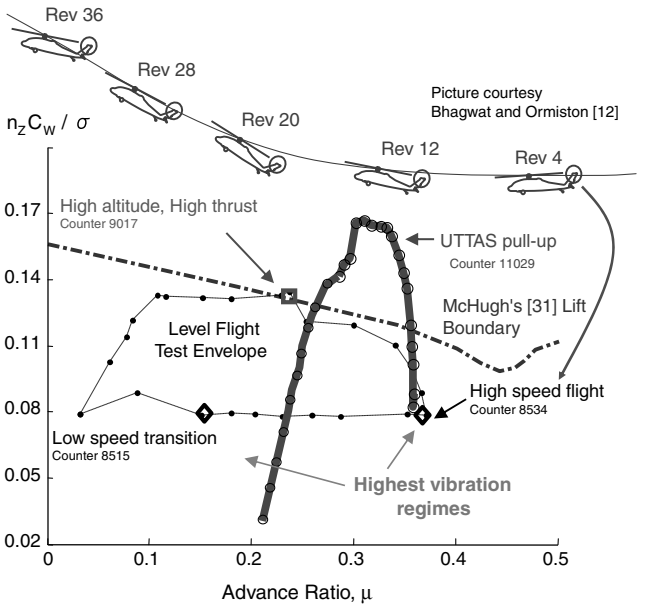

Fig. 8 UH-60A flight envelope and maneuver trajectory (from [11]).

The aircraft undergoes changes in attitudes as well as flight velocities due to changes in flight path. In our approach, the attitude changes are modeled by actually rotating the grids to correspond to the vehicle orientation in space. In the ALE CFD method, the rotational velocities and accelerations caused by attitude changes are computed using second-order discretizations based on grid positions consistent with the geometric conservation law. Note that these rigid motions of the grid system are in addition to the aeroelastic deformations. The linear velocity changes are introduced using the field-velocity approach; that is, the grid velocities at all grid points are changed by the same magnitude and direction as prescribed by the flight dynamics at each time step. Note that these grid velocity changes are added to those introduced by the wake influence.

Figure 9 summarizes the variation of vehicle attitudes and pitch control variation. The angle-of-attack and pitch attitude responses slightly lag the normal load-factor response. The peak load factor of 2.1 g is achieved during revs 15–17, followed by peak pitch angle and angle of attack at revs 19–21. From revolution 19, the normal load factor diminishes gradually to 1 because of the gradual reduction of the aft cyclic input.

Matching the initial thrust level is imperative for obtaining the right aerodynamic operating condition for the rotor blades at the initiation of the maneuver. It was observed that using the measured collective setting in the analysis produced a total thrust deficiency. Possible reasons for this discrepancy include an absence of fuselage modeling in the analysis and measurement offsets in the collective setting. Therefore, the collective control input is adjusted such that initial steady-flight thrust levels are matched between analysis and experiment; that is, the trim procedure is performed only for matching the thrust and not the hub moments. Longitudinal and lateral cyclic controls are prescribed exactly as they were measured in the flight test.

The CFD/CSD analysis of the pull-up maneuver was repeated for 3 sets of CFD grid systems to characterize the grid dependence. Figure 10 shows the comparison of aerodynamic loading and respective execution times for the coarse-, baseline-, and fine-mesh systems. The aerodynamic loading shown represents the portions of the maneuver with the highest angle of attack and the largest amount of flow separation. It can be observed that aerodynamic loading has only very small differences between the baseline- and the fine-mesh systems, indicating favorable grid dependence trends. All results presented in the later sections use the predictions from the fine-mesh simulations.

V. Results and Discussion

A. Rotor Performance

Figure 11 shows the comparison of the predicted rotor thrust compared with the total vehicle thrust computed using the normal load-factor flight measurement. The normal load-factor measurement includes contributions from fuselage/tail forces. The present analysis is restricted only to the rotor system, and the thrust changes caused by the fuselage/tail aerodynamics are not modeled. Therefore, Fig. 11 also includes the calculated rotor thrust obtained

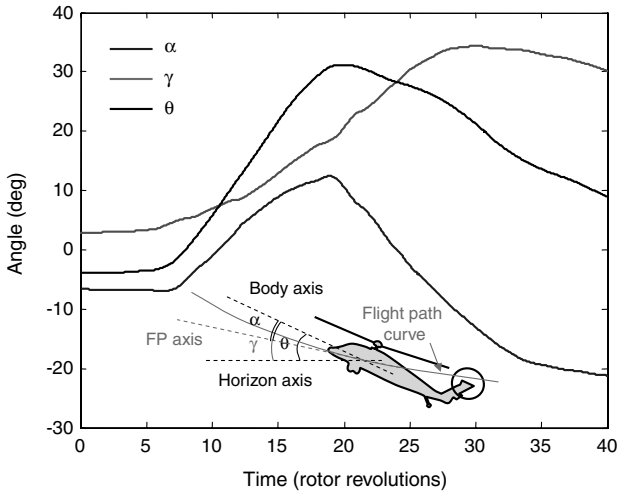

a) Vehicle attitude variation

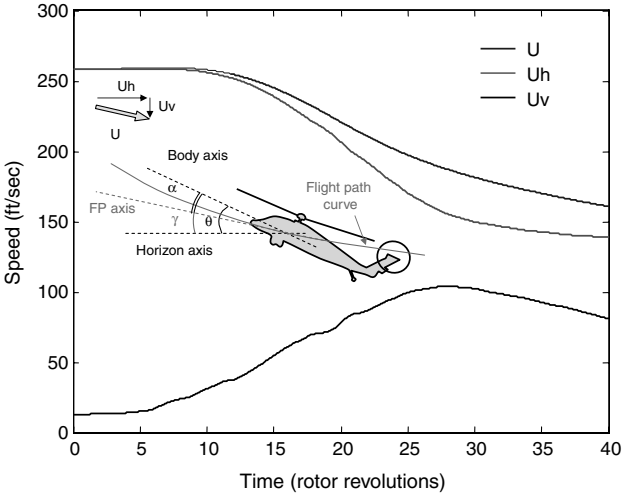

b) Flight-path angle variation

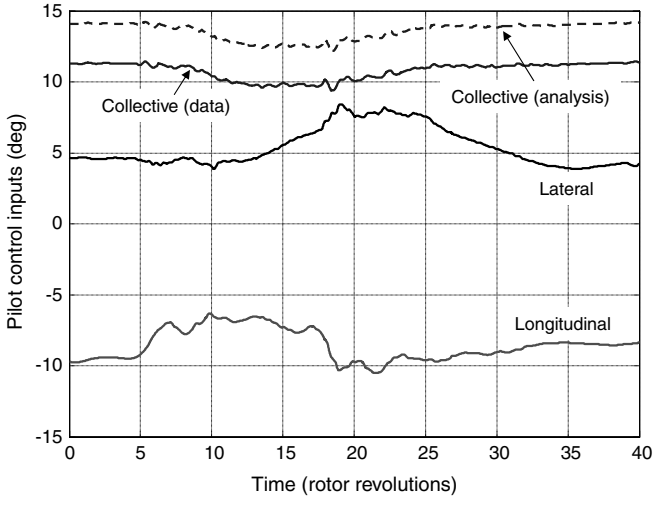

c) Pitch control variation

Fig. 9 Prescribed flight dynamics and controls used for maneuver simulation (FP denotes flight path).

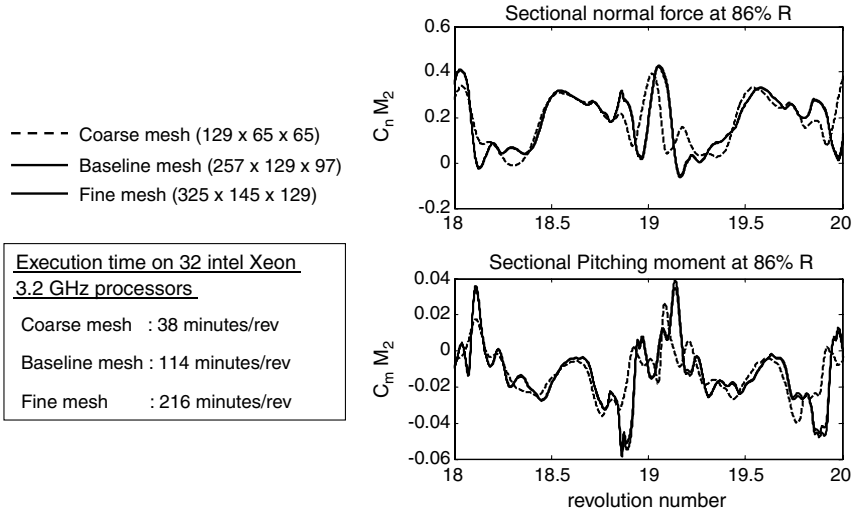

Fig. 10 Grid dependence and performance statistics for the mesh systems used for the simulation.

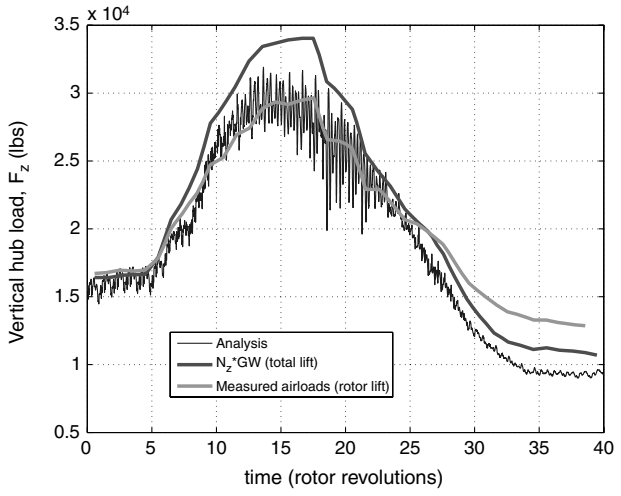

Fig. 11 Predicted vs measured total lift for the entire duration of the pull-up maneuver.

by integrating the measured sectional airloads. The maneuver thrust is plotted as a function of time in units of rotor revolution. The oscillatory nature of the analysis results is because of the combination of unsteady aerodynamic load variations and hub accelerations. The measured data are statistically averaged over every revolution and hence appear smoother. The most prominent features of the lift waveform (rapid increase at the beginning of the maneuver and gradual decrease to steady state at the end of the maneuver) are captured by the analysis. Some discrepancies in the quantitative comparison are expected, because the effects of the fuselage, tail planes, and canted tail rotor are not modeled in the current analysis, which leads to underprediction of the maximum lift. Additionally, the thrust variation during the recovery part of the maneuver is underpredicted by about 30% compared with the thrust integrated from the flight-test aerodynamic loading. Analysis of the rotor lift contours during the last revolution of the maneuver (shown in Fig. 12) indicates lift deficiencies in the analysis around the 0 deg azimuth region, in which the rotor blades interfere with the flow separation from the hub, the engine outlet, and the tail boom flowfield. It is possible that these aerodynamic interferences are significant in the final flight condition of the aircraft, which is a shallow-climb condition. Similar lift deficiency can also be observed in the work by Bhagwat and Ormiston [12], which uses the wake-capturing approach (with overset grids modeling the entire flowfield).

The inaccuracies in lift force prediction indicate that the present methodology is insufficient for coupling directly with flight dynamics for full maneuver simulation. Studies including the aircraft fuselage, engine flowfields, and tail rotor effects are required to understand the lift deficiencies and improve the fidelity of the analysis.

B. Wake Dynamics

The prediction of the unsteady wake dynamics is illustrated in Fig. 13. Predicted vortex wake geometry follows expected qualitative trends corresponding to the prescribed flight dynamics and computed aeromechanics. At the initiation of the maneuver (rev 4), the operating condition is very close to steady high-speed forward flight, in which the wake is convected away from the rotor

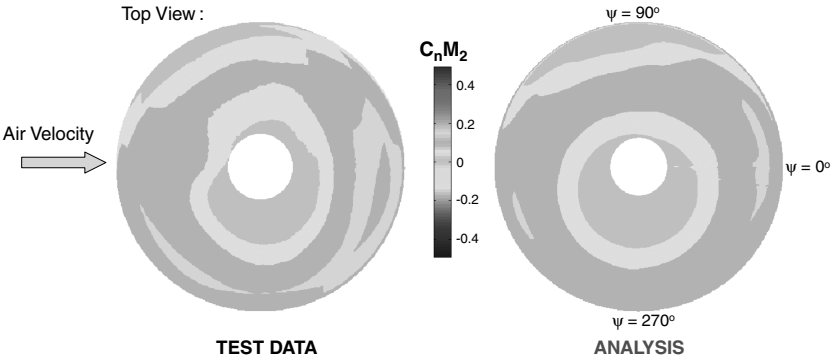

Fig. 12 Contours of rotor lift (sectional normal force) for the last revolution (rev 40) of the pull-up maneuver.

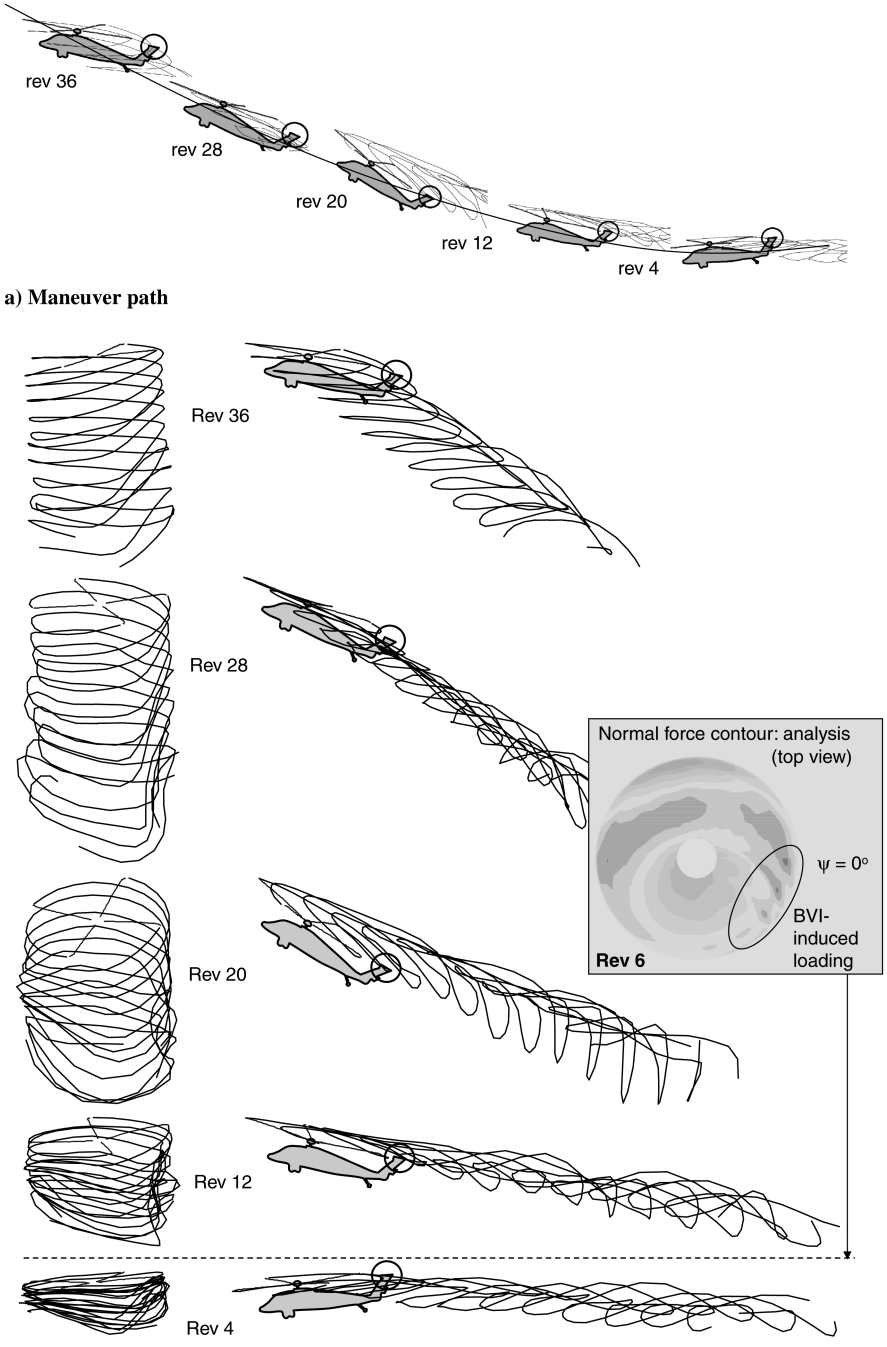

Fig. 13 Snapshots of unsteady wake dynamics during the course of the pull-up maneuver (BVI denotes blade–vortex interaction).

system in the horizontal direction. Returning-wake effects are minimal at this condition. The wake geometry shows asymmetrical roll-up in the rear view because of the large difference in the aerodynamic loading distributions on the advancing and retreating side of the rotor disk.

The aircraft angle of attack rapidly changes from nose-down to nose-up in the next 16 revolutions, with the maximum angle of attack attained at the time level of about 20 revolutions. The vortex wake convects very closely and even cuts through the rotor disk at around revolution 6 during this process. Blade–vortex interactions caused by proximity of the tip vortices can be observed in the lift contours at the sixth revolution (shown as an inset in Fig. 13) of the maneuver. However, the magnitude of the blade–vortex interaction impulses are relatively small compared with the overall thrust level of the aircraft. The aerodynamic loading during the pull-up part of the maneuver (rev 12–20) combines the effects of induced velocities caused by proximity of tip vortices as well as blade stall events. Therefore, the isolated effects of the vortex interactions are not very apparent in the aerodynamic loading. At the maximum-angle-of-attack portion of the maneuver (revolution 20), the combination of high thrust, higher climb rate, and decreased forward speed causes increased vertical convection of the wake.

From revolution 20, the aircraft pitch attitude decreases gradually from its maximum value of 30 deg. The aircraft angle of attack, however, decreases rapidly because of the increase in climb rate. The combination of aircraft pitch change and increased climb rate causes the vortex wake to cut through the rotor disk once again during the course of the maneuver, producing high-frequency aerodynamic loading perturbations of small magnitudes. Toward the end of the maneuver at rev 36 the aircraft is climbing at about two-thirds of its forward speed, causing the wake to be spread vertically. The wake dynamics are benign at this condition because of the reduced thrust levels and a more even aerodynamic loading distribution on the rotor disk.

C. Aerodynamic Loading Prediction

The aerodynamic loading at various instances of the unsteady maneuver are illustrated in Figs. 14–16. Each figure shows the azimuthal variation of sectional normal force and sectional pitching moment (mean removed) at four chosen radial stations.

1. *Sectional Normal Force Prediction*

Overall, the sectional normal force variations are well captured by the analysis for the entire maneuver. The normal force waveforms are dominated by the presence of advancing-side negative lift gradient due to transonics and retreating-side negative lift gradient due to flow separation. Fair prediction of the normal forces indicates that the analysis is able to predict the larger-scale aeromechanics of this flight condition correctly. However, specific details of the waveform are not well captured, particularly the loading impulse on the advancing side, which may be caused by transonic stall. The normal forces are less sensitive to the actual aerodynamic loading along the airfoil, compared with the pitching moments. Therefore, the pitching moment variations constitute a more accurate metric to gauge the quality of the analytical results.

2. *Sectional Pitching Moment Prediction*

At the beginning of the maneuver (Fig. 14), the operating condition is very close to high-speed forward flight. The main characteristics of the waveforms of aerodynamic loading are the presence of negative lift and negative pitching moments on the advancing blade. From Fig. 14 it can be clearly seen that the CFD-based aerodynamics predicts the pitching moment waveform quite accurately. This is because CFD provides accurate modeling of the advancing-blade transonic effects (moving shock and shock relief toward the tip). Accurate prediction of sectional pitching moment leads to improved prediction of the elastic torsional response, leading

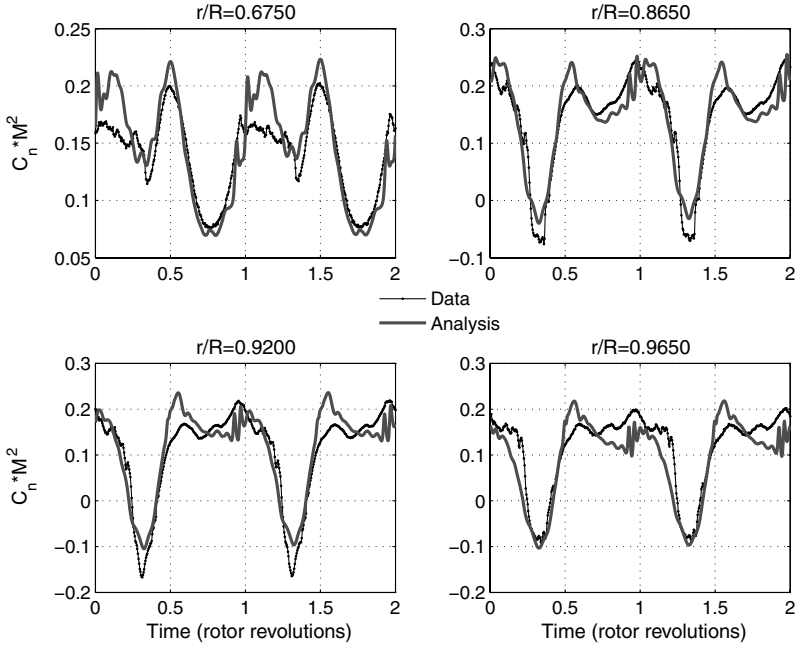

a) Normal force variation

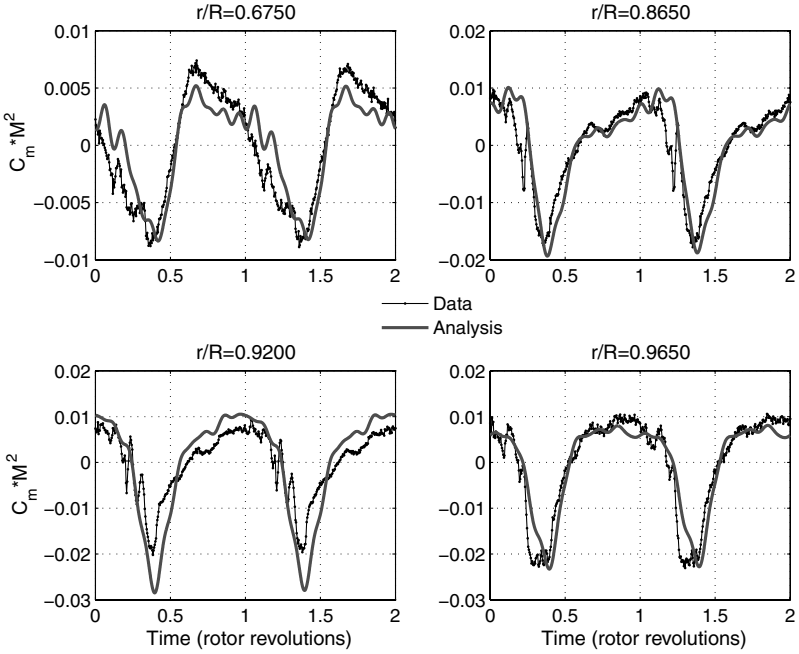

b) Pitching moment variation (mean removed)

Fig. 14 Nondimensional sectional force variation with azimuth for the first two revolutions of the maneuver.

to improved prediction of effective angle of attack (which is a combination of control pitch, elastic torsion, and inflow) at each blade section. Improved prediction of effective angle of attack in turn leads to improved prediction of advancing-blade lift waveform.

As the aircraft engages on the longitudinal pull-up, the pitch attitude and aircraft angle-of-attack increase, leading to an increased thrust. The higher sectional angle of attack caused by the combination of control pitch, aircraft pitch rate, and inflow transients causes flow separation and eventual stall on the retreating side of the rotor. The high-frequency torsional response caused by the impulsive nose-down pitching moment causes an elastic torsional response, which relieves the high angle of attack momentarily, causing the flow to reattach. However, within a few degrees of azimuthal sweep, the elastic torsional response becomes out of phase with the control pitch, inducing a higher sectional angle of attack and leading to another stall event. The presence of these two distinct stall events are most pronounced in revs 12–24 of the maneuver, when the aircraft attains the maximum thrust level. The pitching moment excursions caused by the stall events are clearly visible in the sectional pitching moment plots (Figs. 15b and 16b). The analysis shows fair correlation in the prediction of these stall events. In particular, the magnitudes of the stall events are underpredicted and the second stall cycle shows phase error with the experimental data. There is a third stall event clearly visible in the experimental data on the advancing side of the rotor disk. The analysis only predicts a weak stall event on the advancing side when compared with the experiment. This is consistent with the results obtained by Bhagwat and Ormiston [12]. The inaccuracies in the inflow distribution from the single-tip free-wake model may contribute to this underprediction. Moreover, unsteady RANS computations suffer from large turbulence model

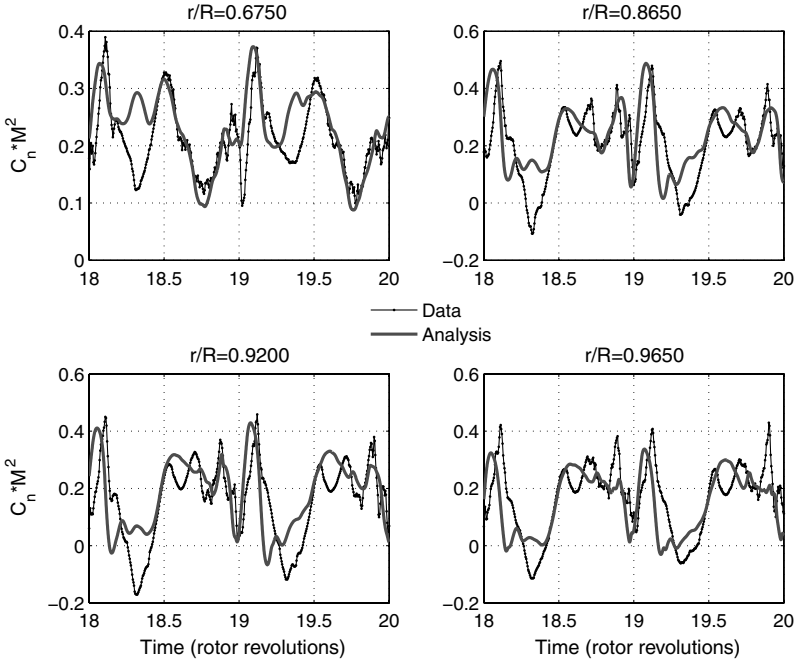

a) Normal force variation

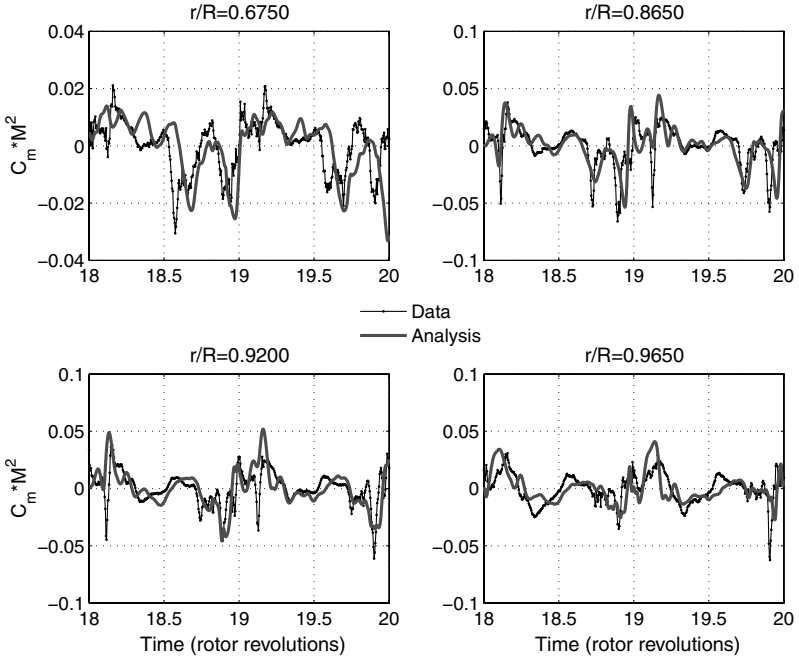

b) Pitching moment variation (mean removed)

Fig. 15 Nondimensional sectional force variation with azimuth for the revs 19–20 of the maneuver.

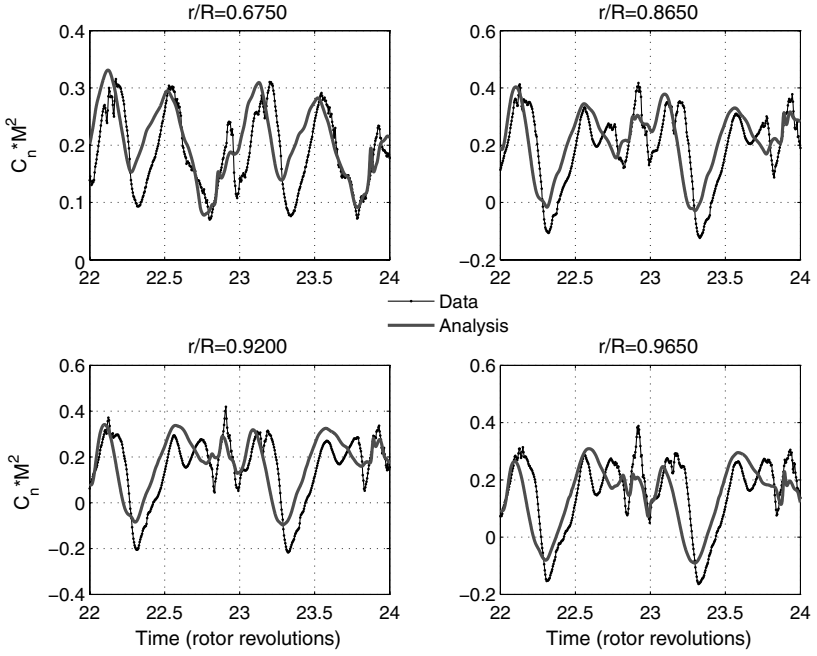

a) Normal force variation

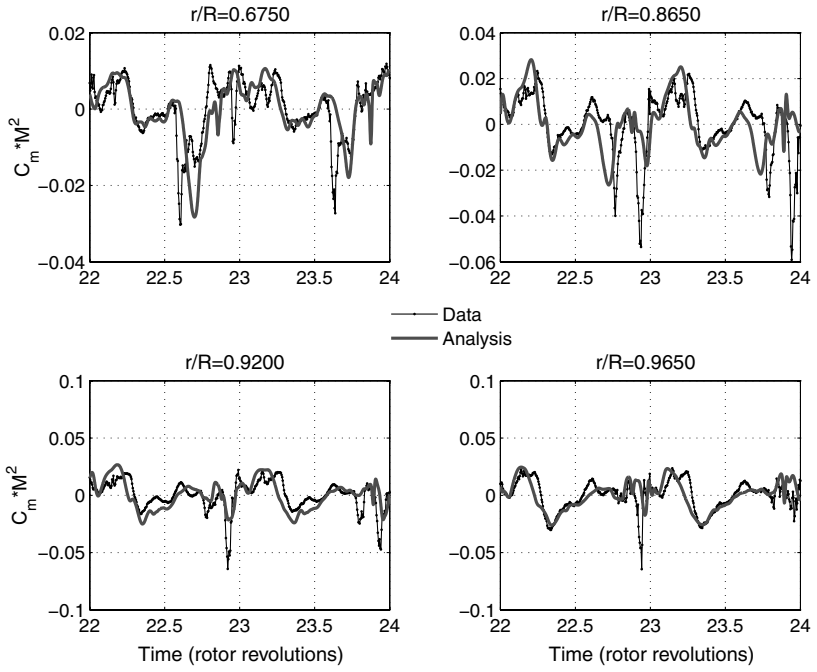

b) Pitching moment variation (mean removed)

Fig. 16 Nondimensional sectional force variation with azimuth for the revs 23–24 of the maneuver.

sensitivities in resolving incidence of separation, reattachment, and shock/boundary-layer interaction, all of which are significant in this case.

As the aircraft recovers from the pull-up, the higher angle of attack is relieved by a nose-down pitching attitude and pitch rate. This results in decreased intensity of the retreating blade stall events and disappearance of the advancing-blade stall event (revolutions 23–24). The analysis shows improved correlation at these instances in resolving the pitching moment waveforms (Fig. 16b).

D. Structural Loading Prediction

Accurate prediction of rotor blade structural loads is important for design considerations and is very challenging for this demanding maneuvering-flight condition.

Three rotating frame loads are presented for comparison with test data: push-rod force, normal bending moment at 50% R, and edgewise bending moment at 50% R. In each case, the variation of the half-peak-to-peak amplitude is presented, followed by the details of the waveform. For clarity and to allow comparison with published flight-test data, the waveform plots are shown only for four selected two-revolution frames spanning the maneuver: revolutions 1–2, 15–16, 19–20, and 23–24.

The pull-up maneuver is known to cause the highest loading on the push-rods (linkages that are used to move the swash plates for pitch control) over the entire operating envelope of the helicopter. Hence, the predicted structural loading on the push rod is an important design criteria for that component. Predicted push-rod loads for blade 1 are shown in Figs. 17 and 18. Figure 17 shows that the peak-to-peak torsion moment trend is predicted satisfactorily; however,

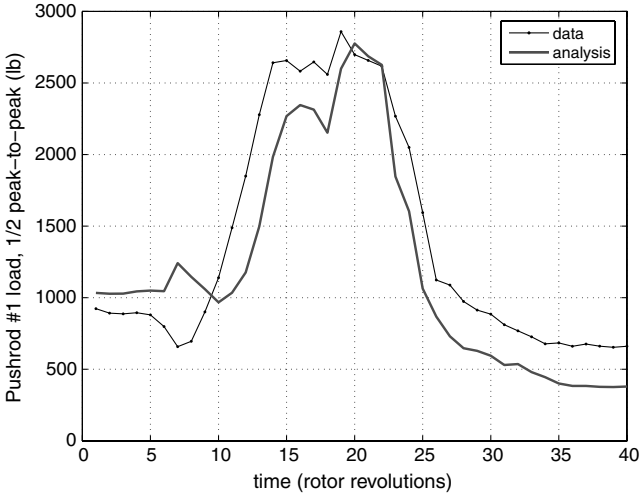

Fig. 17 Push-rod 1 load, half-peak-to-peak variation.

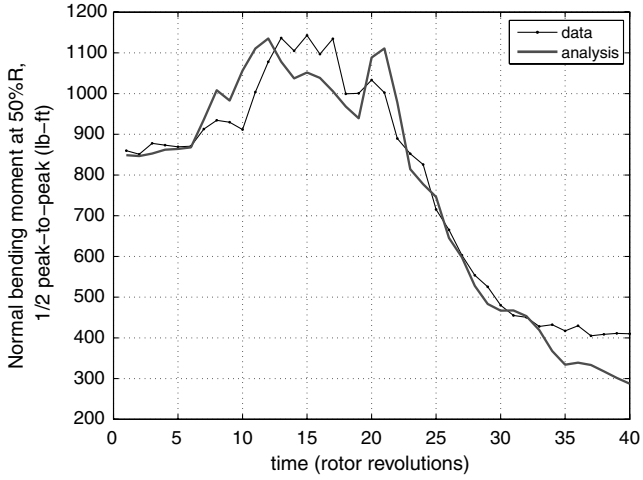

Fig. 19 Normal bending moment at 50% *R*, half-peak-to-peak variation.

the sudden increase in vibratory amplitude that occurs at around rev 7 in the test data is not predicted until rev 12, possibly due to the inaccuracies in stall prediction. However, the maximum push-rod load amplitude is predicted satisfactorily. The details of the waveform for key phases of the maneuver are well captured, as shown in Fig. 18, which clearly shows the large stall-related oscillations on the retreating side under high normal loading, especially for revs 19–20.

Results for the rotor blade normal bending moment at 50% blade radius are shown in Figs. 19 and 20. For this blade load, both the peak-to-peak amplitude variation and details of the waveform are very well predicted, consistent with the accurate prediction of the sectional lift. However, the peak-to-peak amplitude of the normal bending moment is slightly underpredicted at the end of the maneuver (by a factor of 0.7). This is also consistent with the underprediction of final total rotor thrust seen in Fig. 11.

Finally, results for blade edgewise bending moments at 50% blade radius are shown in Figs. 21 and 22. In this case, the peak-to-peak variation trend is captured satisfactorily, with maximum amplitude at around rev 20, but the amplitudes at the start and at the end of the maneuver are quite underpredicted (by a factor of about 0.4). Also, details of the waveform are not very well predicted for the edgewise bending moment compared with the other blade loads.

VI. Conclusions

This paper presented correlation with test data for a tightly coupled fluid–structure analysis simulating a maneuvering-flight condition of the UH60A helicopter. The following conclusions could be drawn on the overall accuracy of the simulation:

1) The total rotor thrust variation during the maneuver is well predicted for the pull-up part of the maneuver, with a peak rotor lift close to 30,000 lb. However, the rotor thrust variation during the recovery part of the maneuver is underpredicted by about 30%.

2) Main features of the sectional lift variation are well predicted compared with flight-test data for the entire duration of the maneuver. Advancing-side transonics and retreating-side flow separation that occurs at high load factors are well captured.

3) Sectional pitching moments are not predicted satisfactorily. The stall events occurring at high load factors on the retreating side of the rotor disk are captured but not resolved accurately; the advancing-side transonic stall is not well captured.

4) Structural loads prediction is good for the normal bending moment at 50% *R* (both peak-to-peak variation and waveform), satisfactory for the torsion moment at 30% *R* and push-rod loads (increase in peak-to-peak amplitude delayed by about 5 revs compared with test data and good waveform prediction), and less than

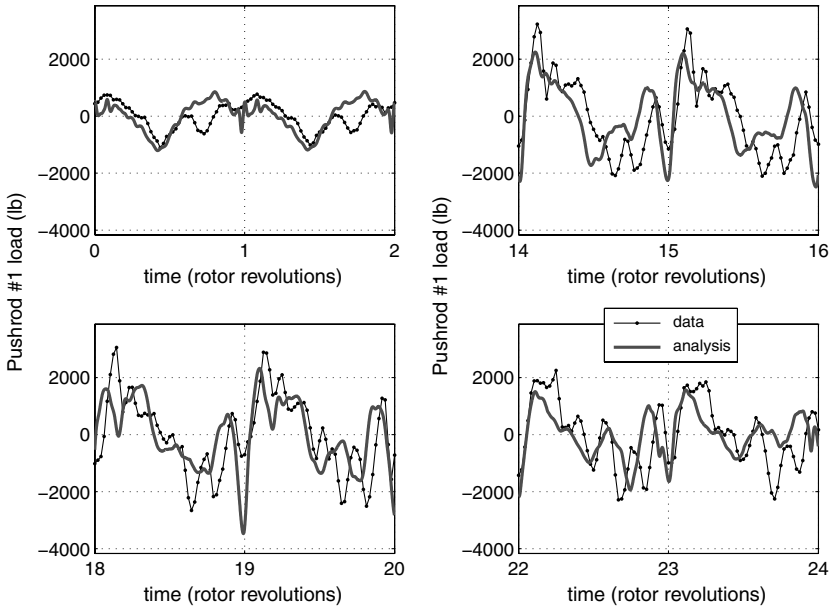

Fig. 18 Push-rod 1 load, time histories (mean removed).

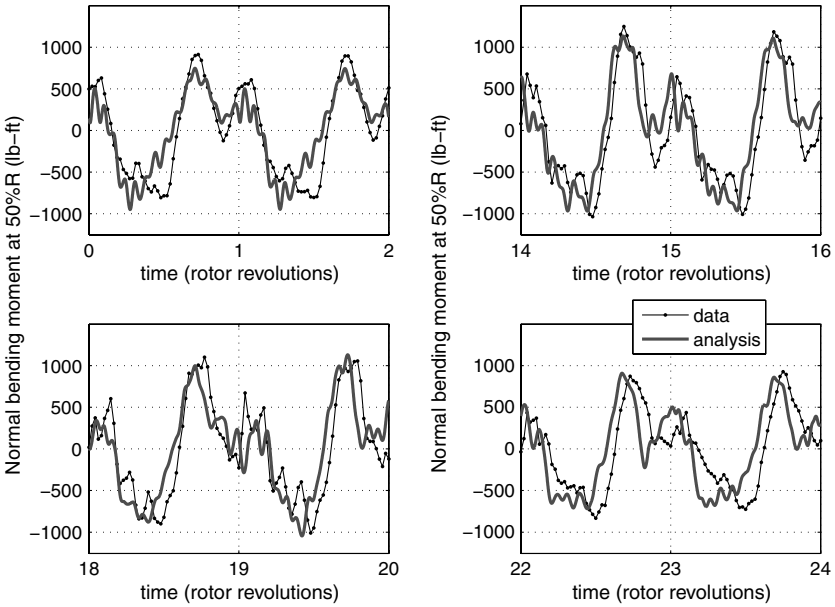

Fig. 20 Normal bending moment at 50% *R*, time histories (mean removed).

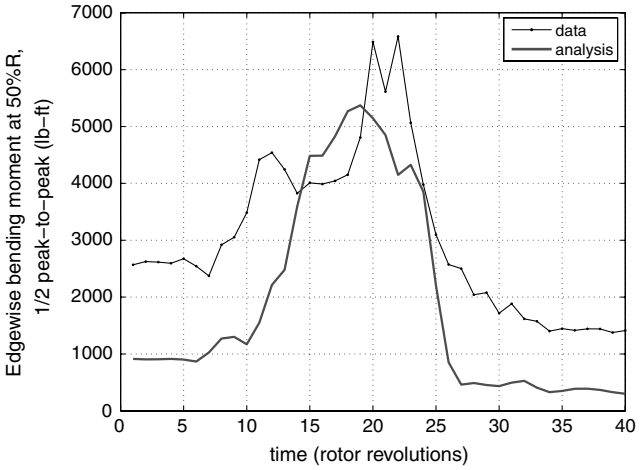

Fig. 21 Edgewise bending moment at 50% *R*, half-peak-to-peak variation.

satisfactory for the edgewise bending moment at 50% *R* (large underprediction of peak-to-peak amplitude).

This paper forms another link in the chain of research looking at improving the state-of-the-art in rotorcraft aeromechanics prediction. The results presented here agree with prior observations and further confirm the efficacy of coupled fluid–structure analysis in predicting aerodynamic and structural dynamic loading behaviors during unsteady maneuvers. Moreover, the present study shows the capability of the wake-coupling approach to produce results with levels of accuracy similar to the wake-capturing approach. The wake-coupling approach may be favored for preliminary design applications because of its faster execution time.

Significant modeling challenges still exist in further improving the prediction of rotorcraft aeromechanics. The most apparent ones that can be noted from the present work are in the prediction of stall onset and reattachment, which needs to be addressed by studies with higher grid resolution as well as improved turbulence modeling. Moreover, current studies of rotorcraft maneuvers are still limited in scope because they rely heavily on measured flight dynamic data. Therefore, another improvement that can be considered is full integration with flight dynamic modeling.

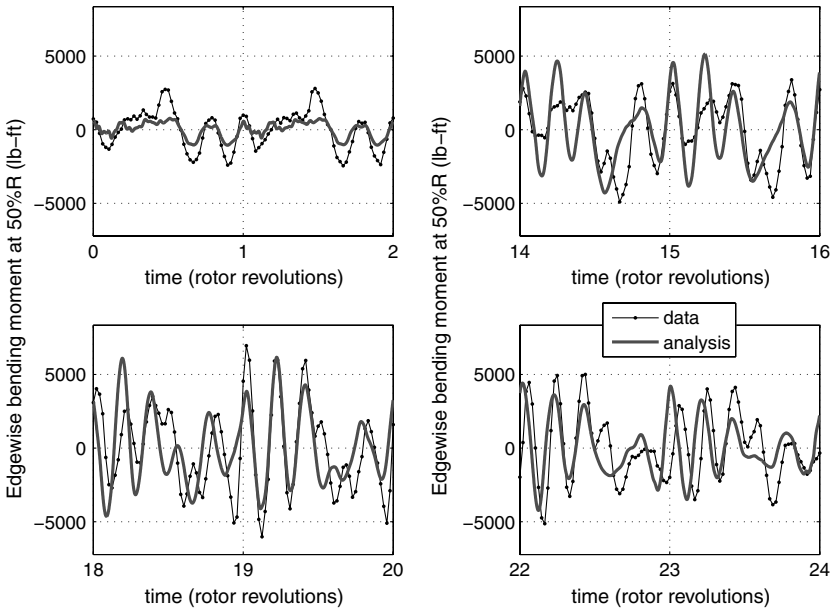

Fig. 22 Edgewise bending moment at 50% *R*, time histories (mean removed).

Acknowledgments

We acknowledge the support from the U.S. Army Research Laboratory with Mark Nixon and Matthew Wilbur as technical monitors. We thank Olivier Bauchau at the Georgia Institute of Technology for providing the DYMORE code. We are grateful to Hyeonsoo Yeo, Mahendra Bhagwat, Robert Ormiston, and Robert Kufeld at NASA Ames Research Center for sharing their thoughts and permitting usage of the published experimental data. We would also like to thank James Baeder and Ben Silbaugh from the University of Maryland for reviewing the paper.

References

[1] Bousman, W. G., "Putting the Aero Back into Aeroelasticity," 8th Annual ARO Workshop on Aeroelasticity of Rotorcraft Systems, University Park, PA, U.S. Army Research Office, Paper A695084, Oct. 1999.

[2] Datta, A., Sitaraman, J., Chopra, I., and Baeder, J., "Analysis Refinements for Prediction of Rotor Vibratory Loads in High-Speed Forward Flight," *American Helicopter Society 60th Annual Forum* [CD-ROM], AHS International, Alexandria, VA, June 2004.

[3] Sitaraman, J., Datta, A., Baeder, I., and Chopra, I., "Coupled CFD/CSD Prediction of Rotor Aerodynamic and Structural Dynamic Loads for Three Critical Flight Conditions," *31st European Rotorcraft Forum* [CD-ROM], Associazione Italiana di Aeronautica e Astronautica, Rome, Sept. 2005.

[4] Potsdam, M., Yeo, H., and Johnson, W., "Rotor Airloads Prediction Using Loose Aerodynamic/Structural Coupling," *American Helicopter Society 60th Annual Forum* [CD-ROM], AHS International, Alexandria, VA, June 2004.

[5] Altmikus, A. R. M., Wagner, S., Beaumier, P., and Servera, G., "A Comparison : Weak Versus Strong Modular Coupling for Trimmed Aeroelastic Rotor Simulation," *American Helicopter Society 58th Annual Forum* [CD-ROM], AHS International, Alexandria, VA, June 2002.

[6] Pomin, H., and Wagner, S., "Aeroelastic Analysis of Helicopter Rotor Blades on Deformable Chimera Grids," *Journal of Aircraft*, Vol. 41, No. 3, May–June 2004, pp. 577–584. doi:10.2514/1.11484

[7] Sitaraman, J., Baeder, J. D., and Chopra, I., "Validation of UH-60 Rotor Blade Aerodynamic Characteristics Using CFD," *59th Annual Forum of the American Helicopter Society* [CD-ROM], AHS International, Alexandria, VA, 2003.

[8] Duraisamy, K., Sitaraman, J., and Baeder, J., "High Resolution Wake Capturing Methodology for Improved Rotor Aerodynamic Computations," *61st Annual Forum of the American Helicopter Society* [CD-ROM], AHS International, Alexandria, VA, 2005.

[9] Sitaraman, J., Baeder, J. D., and Iyengar, V., "On the Field Velocity Approach and Geometric Conservation Law for Unsteady Flow Simulations," 16th AIAA Computational Fluid Dynamics Conference, Orlando, FL, AIAA Paper 2003-3835, June 2003.

[10] Sitaraman, J., and Baeder, J. D., "Evaluation of the Wake Prediction Methodologies Used in CFD Based Rotor Airload Computations," 24th Applied Aerodynamics Conference, San Francisco, AIAA Paper 2006-3472, June 2006.

[11] Bhagwat, M., Ormiston, R., Saberi, H., and Xin, H., "Application of CFD/CSD Coupling for Analysis of Rotorcraft Airloads and Blade Loads in Maneuvering Flight," *63rd Forum of the American Helicopter Society* [CD-ROM], AHS International, Alexandria, VA, 1–3 May 2007.

[12] Bhagwat, M., and Ormiston, R., "Examination of Rotor Aerodynamics in Steady and Maneuvering Flight Using CFD and Conventional Methods," *AHS Specialists Conference on Aeromechanics* [CD-ROM], AHS International, Alexandria, VA, Jan. 2008.

[13] Abhishek, A., Datta, A., and Chopra, I., "Comprehensive Analysis, Prediction, and Validation of UH60A Blade Loads in Unsteady Maneuvering Flight," *AHS Specialists Conference of the American Helicopter Society* [CD-ROM], AHS International, Alexandria, VA, Jan. 2008.

[14] Silbaugh, B., and Baeder, J. D., "Coupled CFD/CSD Analysis of a Maneuvering Rotor Using Staggered and Time-Accurate Coupling Schemes," *AHS Specialists Conference on Aeromechanics* [CD-ROM], AHS International, Alexandria, VA, Jan. 2008.

[15] Srinivasan, G. R., and Baeder, J. D., "TURNS: A Free-wake Euler/Navier–Stokes Numerical Method for Helicopter Rotors," *AIAA Journal*, Vol. 31, No. 5, 1993, pp. 959–962. doi:10.2514/3.49036

[16] Bauchau, O. A., and Kang, N. K., "A Multibody Formulation for Helicopter Structural Dynamic Analysis," *Journal of the American Helicopter Society*, Vol. 38, No. 2, Apr. 1993, pp. 3–14. doi:10.4050/JAHS.38.3

[17] Jameson, A., and Yoon, S., "Lower-Upper Implicit Schemes with Multiple Grids for the Euler Equations," *AIAA Journal*, Vol. 25, No. 7, 1987, pp. 929–935. doi:10.2514/3.9724

[18] Yoon, S., and Jameson, A., "An LU-SSOR Scheme for the Euler and Navier Stokes Equations," 25th Aerospace Sciences Meeting, AIAA Paper 1987-600, Reno, NV, Jan. 1987.

[19] Vinokur, M., "An Analysis of Finite-Difference and Finite-Volume Formulations for Conservation Laws," *Journal of Computational Physics*, Vol. 81, No. 1, Mar. 1989, pp. 1–52. doi:10.1016/0021-9991(89)90063-6

[20] Pulliam, T., and Steger, J., "Implicit Finite Difference Simulations of Three Dimensional Compressible Flow," *AIAA Journal*, Vol. 18, No. 2, 1980, pp. 159–167. doi:10.2514/3.50745

[21] Bauchau, O. A., Bottasso, C. L., and Trainelli, L., "Robust Integration Schemes for Flexible Multibody Systems," *Computer Methods in Applied Mechanics and Engineering*, Vol. 192, No. 3–4, 2003, pp. 395–420. doi:10.1016/S0045-7825(02)00519-4

[22] Peters, D. A., and He, C. J., "Finite State Induced Flow Models. Part 2: Three-Dimensional Rotor Disk," *Journal of Aircraft*, Vol. 32, No. 2, Mar.–Apr. 1995, pp. 323–333. doi:10.2514/3.46719

[23] Bhagwat, M., and Leishman, J. G., "Stability, Consistency and Convergence of Time-Marching Free-Vortex Rotor Wake Algorithms," *Journal of the American Helicopter Society*, Vol. 46, No. 1, Jan. 2001, pp. 59–71. doi:10.4050/JAHS.46.59

[24] Roget, B., "Simulation of Active Twist and Active Flap Control on a Model-Scale Helicopter Rotor," 24th Applied Aerodynamics Conference, San Francisco, AIAA Paper 2006-3473June 2006.

[25] Squire, H. B., "The Growth of a Vortex in Turbulent Flow," *Aeronautical Quarterly*, Vol. 16, Aug. 1965, pp. 302–306.

[26] Weissinger, J., "The Lift Distribution on Swept-Back Wings," NACA TM 1120, Mar. 1947.

[27] Datta, A., "Fundamental Understanding, Prediction, and Validation of Rotor Vibratory Loads in Steady Level Flight," Ph.D. Thesis, Univ. of Maryland, College Park, MD, 2004.

[28] Kufeld, R. M., and Johnson, W., "The Effects of Control System Stiffness Models on the Dynamic Stall Behavior of a Helicopter," *American Helicopter Society 54th Annual Forum* [CD-ROM], AHS International, Alexandria, VA, 20–22 May 1998.

[29] Bousman, G., Kufeld, R. M., Balough, D., Cross, J. L., Studebaker, K. F., and Jennison, C. D., "Flight Testing the UH-60A Airloads Aircraft," *50th Annual Forum of the American Helicopter Society* [CD-ROM], AHS International, Alexandria, VA, May 1994.

[30] Kufeld, R. M., "High Load Conditions Measured on a UH-60A in Maneuvering Flight," *Journal of the American Helicopter Society*, Vol. 43, No. 3, July 1998, pp. 202–211. doi:10.4050/JAHS.43.202

[31] McHugh, F. J., "What are the Lift and Propulsive Force Limits at High Speed for the Conventional Rotor?" *American Helicopter Society 34th Annual Forum* [CD-ROM], AHS International, Alexandria, VA, May 1978.